

ERRORS IN LIGHTNING DIRECTION FINDING BY AIRBORNE CROSSED LOOPS



Lee W. Parker

Lee W. Parker, Incorporated, Concord, Massachusetts

AD P002208

ABSTRACT

Analytical and computer approaches are presented for predicting the site errors of airborne crossed loops used for lightning direction-finding. This type of azimuth error is caused by distortion of the incident field due to induced skin currents. Computer code results are presented for a T-39 and a C-130 aircraft used in flight-testing a commercial crossed-loop system. Another type of bearing error, caused by non-vertical lightning channels, is analyzed for the case where both detector and lightning source are above a conducting ground plane. Also discussed is the 180-degree ambiguity and its resolution by an electric field antenna.

AIRBORNE CROSSED LOOPS may be used to sense the azimuth of lightning discharges as an on-board aid in the avoidance of thunderstorm regions. However, the loops can be susceptible to serious site errors in lightning direction-finding, depending on the geometry of the aircraft and the loop location on it (1, 2, 3)*. These site errors are caused by scattering (re-radiation due to induced eddy currents) of the incident magnetic wave field by nearby conducting surfaces (the skin of the aircraft). These eddy currents produce a secondary magnetic field that results in a total magnetic vector of generally different (distorted) orientation from the incident orientation. The crossed-loop detector is "misdirected" when it senses the distorted orientation and indicates an erroneous bearing. (The term "misdirection" was used earlier in this sense, and may have been coined by A. Sommerfeld (13).) Another consequence of the site error is that it disturbs also lightning ranging systems that use relations between magnetic amplitude and distance, since the amplitude as well as the direction is distorted by the scattering effect.

Two approaches, analytical and numerical, are presented for analyzing and predicting the site errors of airborne crossed loops. In both approaches we assume that the aircraft is small compared with the radiation wavelength (magnetostatic limit), and solve Laplace's equation to obtain the scattered magnetic field vector, for arbitrary azimuth angles of incidence of the wave from the lightning radiation source. The site error arises from the fact that the individual orthogonal magnetic field components are changed by different factors. The error analyses presented here and in Refs. (1) and (2) do not appear to have been published previously.

In the analytic approach, fuselages, wings and tails are modeled by ellipsoids. An important analytical result is that large errors in lightning direction-finding can occur (e.g., of the order of 20°) even in the case where the instrument is symmetrically located, e.g., centered on a long fuselage. The error can be still larger if the instrument is mounted near the nose or tail, or near edges. (See Ref. 3.)

In the numerical approach, the aircraft geometry is modeled realistically, and numerical solutions are obtained using a 3-D computer code. Computational results are presented for two actual aircraft, a T-39 Sabreliner and a C-130 Hercules. These aircraft have been used in flight tests to evaluate a commercially-available crossed-loop system for severe weather avoidance (4, 5, 5). The predicted errors (of the order of 10° for the T-39 and 20° for the C-130) are consistent with flight-test results for the particular mounting locations chosen. The calculations indicate that other locations would reduce the error.

By a combination of theory and experiment, one may determine correction factors for site

errors affecting crossed loops, for any given airplane geometry. The results of this determination would suggest optimum locations for the placement of the loops on the aircraft. The correction factors need be determined only once. If this is done, the site errors can be completely eliminated by suitable adjustment of the electronic amplification.

Also discussed are azimuth errors due to non-vertically-polarized lightning channels, and the 180-degree ambiguity inherent in crossed loops. A non-vertical (or "slant") lightning channel will cause a crossed loop to determine an erroneous direction, if the loop and lightning channel are at different altitudes. The effects of loop altitude above a conducting ground plane (as opposed to lightning altitude) on azimuth (or bearing) errors do not appear to have been considered in the literature. An analytical formula is derived, generalizing results obtained for zero loop altitude (9, 10) to the case of finite altitude.

The use of an electric antenna in conjunction with the loop to resolve the 180-degree ambiguity by correlating the phases of the electric and magnetic vectors is an important problem, and is considered in the Appendix. It is clear that low signal-to-noise ratios or unintentional phase shifts in the electronic amplifiers can produce 180-degree errors.

ANALYTICAL APPROACH

Evaluation of the scattering of incident electromagnetic waves is generally a difficult problem, even for perfectly conducting bodies of simple shape, e.g., spheres (7). If we assume that the radiation wavelength is larger than the dimension of the airplane, the problem is simplified because Maxwell's equations are replaced by the Laplace equation of magnetostatics. This approximation is valid for frequencies below the first aircraft resonance, i.e., for frequencies below about one MHz (8). In the magnetostatic limit, the boundary condition at the aircraft surface is that the magnetic field be tangent to the surface (zero normal gradient, a Neumann boundary condition). That is, the magnetic field is excluded from the interior of the aircraft by the induced skin currents. This boundary condition is justifiable based on the fact that the skin depth (given by $66/\nu^{1/2}$ in mm for copper, where ν is the frequency in Hz (7)) is only 0.3 mm at the frequency 50 kHz of interest here, and is therefore less than typical aircraft skin thicknesses (at least one mm).

In magnetostatics the magnetic field vector at any point may be expressed as the gradient of a scalar potential function ϕ , where ϕ satisfies the Laplace equation in the region exterior to the airplane, has a vanishing normal derivative on the airplane surface, and asymptotically approaches a linear form (constant gradient) at infinity.

For analytical purposes (as opposed to the numerical approach discussed later for realistic

* Numbers in parentheses designate references at the end of paper.

geometries) it is convenient to model the aircraft by a single geometric form. Since the Laplace equation is separable in ellipsoidal coordinates, a versatile 3-D form that can be defined by one coordinate of a 3-parameter ellipsoidal coordinate system is the tri-axial ellipsoid. Here solutions are expressed in elliptic integrals, that need special tables or computer programs for numerical evaluation. However, if we specialize the ellipsoid to a bi-axial (rotationally symmetric) prolate spheroid or to an elliptical cylinder, simpler solutions expressed in terms of trigonometric functions (arc tangent) are obtained. In many cases these simplified mathematical models are sufficient to study conditions on the edges of the wings and on the tail (using the elliptic cylinder) and conditions on the fuselage (using the prolate spheroid). When we specialize to a circular cylinder the difference in the induced surface fields due to the separate orthogonal components of an incident field vector (the cause of the site error) is still significant, as will be shown. However, if we specialize further to a sphere this difference vanishes because of the extreme symmetry of the sphere (see e.g. Table 1). Therefore, the sphere has no site error and cannot be used to model the misdirection effect of an airplane body.

Consider an ellipsoid representing an airplane or a part thereof. Figure 1 shows the ellipsoid projected onto the x-y plane of a cartesian coordinate system. It is aligned with the 3 axes, and has semi-axis lengths a, b, and c along the x, y and z axes, respectively. (The z axis is not shown.) We assume that the top of the airplane body points in the +z direction, and that the incident magnetic field is parallel to the x-y plane. The incident wave propagates with angle of attack θ_0 with respect to the y-axis as shown, and with the magnetic field lines perpendicular to this direction. One can consider the magnetic field distortions at several points, such as A, B, C, and D in the figure. These can represent for example positions along the centerline on top of a fuselage or vertical stabilizer and rudder ("tail fin"), or along a wing or horizontal stabilizer and elevator.

Later we will consider the axially symmetric case in which the y-axis is the axis of rotational symmetry. Thus we consider the solution to be a superposition of the two primary solutions: One is the "transverse" case where $\theta_0=0^\circ$, the incident field being in the x-direction, perpendicular to the axis of symmetry. The other is the "axial" case where $\theta_0=90^\circ$, in which the incident field is in the y-direction, parallel to the axis of symmetry.

Before considering the spheroid, let us first consider the limit in which b becomes infinite. The ellipsoid then elongates into a long cylinder or wire parallel to the y-axis and of constant elliptic cross-section, as shown in Fig. 2.

CIRCULAR CYLINDER (c=a)

Here we treat the circular cylinder, where $c=a$ and $b=\infty$, first in the axial case where $\theta_0=90^\circ$. In this case the field is parallel to the cylinder axis, and the solution becomes trivial. The field is excluded from the interior by a solenoidal sheet current in the surface, in the azimuthal direction about the axis. This current produces an internal field that cancels out the incident field, but the current produces no external field. Hence there is no distortion in the axial case, $\theta_0=90^\circ$.

Next we treat the circular cylinder in the transverse case, where $\theta_0=0^\circ$. Figure 3a shows the field ("flow") lines in this case. The solution of Laplace's equation that satisfies the boundary conditions at infinity and on the surface is the potential function

$$\phi = -B_0 \cdot (r + a^2/r) \cdot \cos\psi \quad (1)$$

where r denotes the cylindrical radial coordinate, a denotes the cylinder radius, B_0 denotes the magnetic field magnitude at infinity (large r), and ψ is the azimuthal angle about the cylinder axis ($\psi=0$ along the direction of B_0). It may be readily verified that the potential defined by Eq. (1) satisfies Laplace's equation in cylindrical coordinates:

$$\frac{\partial^2 \phi}{\partial r^2} + \frac{1}{r} \frac{\partial \phi}{\partial r} + \frac{1}{r^2} \frac{\partial^2 \phi}{\partial \psi^2} = 0 \quad (2)$$

One boundary condition is that as r becomes large, ϕ approaches

$$\phi \sim -B_0 r \cos\psi = -B_0 x \quad (3)$$

representing the potential of the constant field B_0 along the x-direction. On the surface the other boundary condition is that the normal component of the gradient vanishes, that is,

$$-\frac{\partial \phi}{\partial r} = +B_0 \left(1 - \frac{a^2}{r^2}\right) \cos\psi \quad (4)$$

vanishes for all ψ when $r=a$. Thus Eq. (1) satisfies both boundary conditions.

The radial and azimuthal field components, B_r and B_ψ , are given by the components of the gradient,

$$B_r = -\frac{\partial \phi}{\partial r} = B_0 \cdot \left(1 - \frac{a^2}{r^2}\right) \cdot \cos\psi \quad (5)$$

$$B_{\psi} = -\frac{1}{r} \frac{\partial \phi}{\partial \psi} = -B_0 \left(1 + \frac{a^2}{r^2}\right) \sin \psi \quad (6)$$

The distorted field of interest is obtained by considering the x-component B_x at $r=a$, namely,

$$\begin{aligned} (B_x)_a &= B_r \cos \psi - B_{\psi} \sin \psi \\ &= B_0 + B_0 (2 \sin^2 \psi - 1) (a^2/r^2) \\ &= B_0 + (2 \sin^2 \psi - 1) B_0 \end{aligned} \quad (7)$$

where the first term on the right-hand side of Eq. (7) represents the undisturbed field, and the second term represents the distortion caused by the cylinder.

Thus, the perturbation field (addition to the incident field) goes from $-B_0$ on the "side" looking into the magnetic field, to $+B_0$ on the "top" of the cylinder (where the dot in Fig. 3 represents the probable position of the crossed loop), as ψ increases from 0 to $\pi/2$. Assuming the crossed loop to be normally positioned (at the dot position) on "top", it senses a total field value $2B_0$, that is, the incident value enhanced by a factor 2.

Now we are in a position to calculate the misdirection at angle of attack θ_0 . On top of the cylinder B_x is enhanced by a factor 2, while B_y remains unaffected. Hence we have

$$\frac{B_y}{B_x} = \tan \theta = \frac{B_{oy}}{2B_{ox}} = \frac{1}{2} \tan \theta_0 \quad (8)$$

as the definition of the apparent angle of incidence, θ , and therefore

$$MD \equiv \theta - \theta_0 = \arctan\left(\frac{1}{2} \tan \theta_0\right) - \theta_0 \quad (9)$$

is the amount of misdirection or bearing error at angle of attack θ_0 .

From Eq. (9) we deduce that the bearing error is zero (i.e., $\theta = \theta_0$) when $\theta_0 = 0$ and when $\theta_0 = 90^\circ$. The maximum error is -19.5° (or $+19.5^\circ$) occurring when θ_0 is 54.7° (or its supplement 125.3°). This follows from the vanishing of the derivative of MD with respect to θ_0 . The variation of bearing error with angle θ_0 given by Eq. (9) is shown in the "needle limit" column of Table 1. These results are consistent with ADF loop antenna calibrations shown in Ref. (3).

At arbitrary angle of attack θ_0 , the axial field component gives rise to skin currents flowing azimuthally around the cylinder, while the transverse field component gives rise to longitudinal currents, in the $\pm y$ directions on the two x-sides of the cylinder. Thus the resultant skin current flow-lines are ellipses

whose planes are parallel to the z-axis and the direction of attack (i.e., skewed with respect to the cylinder axis, as shown in Fig. 2).

ELLIPTIC CYLINDER

In the more general elliptic cylinder case ($c \neq a$), the two principal fields are again in the x-direction ($\theta_0 = 0^\circ$, transverse), and the y-direction ($\theta_0 = 90^\circ$, axial). Again as in the circular cylinder, the axial field gives rise to no perturbation. In the transverse case, however, the field lines are perturbed as shown in Fig. 3, where in Figs. 3b and 3c the lines are topologically similar to the circular case, Fig. 3a. Figure 3b ($c < a$) can represent a flat wing, with the crossed loop (large dot in the middle) sensing relatively little field distortion. Figure 3c ($c > a$) can represent a tail fin, where the crossed loop (large dot on the edge) senses a large distortion.

It can be shown that for all cases in Fig. 3 the misdirection is given by

$$MD \equiv \theta - \theta_0 = \arctan(R \tan \theta_0) - \theta_0 \quad (10)$$

where the "ratio-factor" R is defined by

$$R = \frac{a}{a+c} \quad (11)$$

Thus, R reduces to 1/2 when $c=a$ as in Fig. 3a, and Eq. (10) reduces to Eq. (9) for the circular cylinder. At the middle of a flat wing (Fig. 3b) where $c \ll a$, R reduces to approximately unity so that the distortion is minimal. On the edge of a tail fin (Fig. 3c) where $c \gg a$, R becomes small and θ becomes zero (due to the dominance of B_x which becomes large), independent of θ_0 . Thus the distortion is equal to $-\theta_0$ and becomes large at angles near 90° (except at 90°).

PROLATE SPHEROID

A prolate spheroid is a reasonable model for a fuselage of finite length. In this case (referring to Fig. 1, where y is now the axis of rotation), the radii are related by $a=c$, as in the circular cylinder, but b is now finite. Hence the results depend on the aspect ratio $t=a/b$, which is less than unity for a prolate spheroid (and greater than unity for an oblate spheroid). The incident direction angle $\theta_0 = 0^\circ$ if the direction of incidence is parallel to the long axis, and $\theta_0 = 90^\circ$ if the direction of incidence is perpendicular to the long axis.

It can be shown that the ratio-factor R in Eqs. (10) and (11) is now replaced by GR (see Eq. (15) below), where G is defined by

$$G(y,t) = (b^2 - y^2)^{1/4} / (b^2 - y^2 + t^2 y^2)^{1/4} \quad (12)$$

where $t=a/b$, and y is the y-distance of the

surface point from the mid-point; and R may be defined by

$$R(t) = 0.5 (1 - 2t^2 + N)/(1 - N) \quad (13)$$

with N defined by

$$\frac{c^2}{2s} \ln \left(\frac{1+s}{1-s} \right) \quad (14)$$

and $s = (1-t^2)^{1/2}$. Thus the misdirection angle is given by

$$MD \equiv \theta - \theta_0 = \arctan (GR \tan \theta_0) - \theta_0 \quad (15)$$

where G and R are given by Eqs. (12) and (13). Note that G denotes the cosine of the tilt angle β of the tangent-plane with respect to the horizontal plane. Note also that $G=1$ for $y=0$ (the crossed loop is centered on the fuselage).

As the aspect ratio varies from the "needle" limit $t \rightarrow 0$ (an infinitely-long circular cylinder) to the opposite limit $t \rightarrow 1$ (sphere), the factor R varies from 0.5 to 1.0. Assuming the crossed loop to be centered on the fuselage ($G=1$), the misdirection angle $MD = \Delta\theta$ is tabulated as a function of θ_0 in Table 1, for values of $t=0, 0.1, 0.2, 0.5$ and 1.0 . (The corresponding values of R are 0.5, 0.5207, 0.5591, 0.7100 and 1.0.) Note that $MD=0$ if $\theta_0=0^\circ$ or 90° in all cases, and has a maximum magnitude for θ_0 somewhere between 0° and 90° .

As the aspect ratio t increases the largest MD magnitude decreases from its value of 19.5° for an infinitely-long circular cylinder. Thus, if the crossed loop is centered on an F-106 Delta Dart, which may be approximately modeled by a prolate spheroid with aspect ratio $t=0.1$, the largest MD magnitude is predicted to be 18.4° by Table 1, and occurs at $\theta_0=55^\circ$. If the aircraft is a C-130, characterizable by t between 0.1 and 0.2 (but assuming $t=0.2$) the largest MD is 16.4° , occurring at $\theta_0=55^\circ$. As t increases further (as the fuselage becomes thicker compared with its length), the maximum MD decreases toward zero, while the corresponding θ_0 moves slowly toward 45° . In all cases the errors increase if the loop position is moved off center toward the nose or tail. Reference (2) presents further tabulations of Eq. (15) for off-center positions, such as A, B, C, and D in Fig. 1.

REALISTIC NUMERICAL MODELS

For detailed realistic geometries, computer methods must be employed. Our 3-D computer model numerically solves the Laplace equation, in integral form, by a method of moments, subject to the boundary conditions of uniform field

at infinity, and zero normal gradient at the aircraft surface. The aircraft surface is approximated by a large number of small quadrilateral "panels" or "patches", as illustrated in Figs. 4 and 5. (Our code was adapted from a fluid-flow code due to J. L. Hess.) It should be noted that the problems treated here are equivalent to the problems of error compensation encountered in the calibration of low-frequency ADF antennas for aircraft (3).

In the light of data obtained in 1977 and 1981 by the Air Force in flight tests of a Stormscope crossed loop (4, 5, 6), we applied our computer code to obtain a preliminary assessment of the possible influence of site errors. The 1977 tests (4, 5) involved a T-39 Sabreliner, with the instrument installed near the leading edge of (and on the underside of) the right wingtip. The model portrayed in Fig. 4 shows the wing modeled reasonably realistically, while the fuselage, whose detailed structure should be unimportant in this case, is modeled crudely. The 1981 tests (6) involved a C-130 Hercules, with the instrument located under the fuselage near the tail and close to the cargo door. The detailed structure was modeled numerically as illustrated in Fig. 5. In this case we require realistic modeling of the fuselage and tail structure.

We consider first the T-39 results, and then those for the C-130.

T-39 MODEL - The panels in Figs. 4a and 4b are labelled by letters A-H, denoting various sections, with A and B on the fuselage, and C-G on the wing and H on the wingtip. Each section has 12 panels, with Nos. 1-6 on the upper surface and Nos. 7-12 denoting image positions on the under surface (with 7 under 6, 8 under 5, ..., and 12 under 1). The Stormscope instrument position is on Panel G-11, as indicated.

Some selected preliminary results are as follows, indicating panel location, maximum misdirection, and angle of incidence at which this occurs. For each section we give the optimum location.

- A-9: $+11^\circ$ at 135° (bottom of fuselage at midwing)
- B: (no good location, vertical plane)
- C-3: $+16^\circ$ at 30° (top of wing, behind leading edge)
- C-10: $+18^\circ$ at 5° (bottom of wing, behind leading edge)
- D-2: $+8^\circ$ at 15° (top of wing, adjacent to leading edge)
- D-11: $+12^\circ$ at 5° (bottom of wing, adjacent to leading edge)
- E-11: $+5^\circ$ at 15° (bottom of wing, adjacent to leading edge)
- E-2: $+10^\circ$ at 160° (top of wing, adjacent to leading edge)
- F-5: $+3^\circ$ at 110° (top of wing, ahead of trailing edge)
- F-10: $+3^\circ$ at 25° (bottom of wing, behind leading edge)

- G-10: $+4^\circ$ at 80° (adjacent to wingtip, bottom, behind leading edge)
 G-3: $+6^\circ$ at 115° (adjacent to wingtip, top, behind leading edge)
 G-11: -7° at 170° (Stormscope location, bottom, leading corner of wingtip)
 G-2: $+10^\circ$ at 95° (mirror of Stormscope location, top surface)

H: (no good location, vertical plane)

The foregoing represent optimum locations (where the misdirections are minimal). The misdirections are larger at other locations.

The following conclusions may be drawn. The optimum fuselage location is underneath, at midwing position. The optimum locations on the wing (and in fact on the whole airplane) are near the wingtip and away from the fuselage, either on top and ahead of the trailing edge, or underneath and behind the leading edge. The actual Stormscope location used was a reasonable choice (in the absence of data on site errors) but could have been improved. The reported bearing discrepancies (5) are consistent with the computed maximum misdirection near the wingtip, of the order of 10° .

It should be mentioned that these figures apply to an incident field lying entirely in the horizontal plane. The presence of a vertical field component would be associated with a slanted lightning channel. In this way the error due to slant would be coupled with site error. It is straightforward to include the vertical component in the calculations, i.e. to study the site errors associated with slanted channels.

C-130 MODEL - The geometry of the C-130 was simulated as illustrated in Fig. 5. The location of the Stormscope, just aft of the cargo door, is indicated in Fig. 5 by a darkened panel. Some detailed small structures such as engine pods have been omitted in this preliminary work on the assumption that such small structures are sufficiently remote from the particular location of interest that their contributions should be negligible.

At the Stormscope location the maximum bearing error or misdirection (MD) is predicted to be approximately 20° . This error is experienced for incident lightning wave direction 55° (left or right) from the forward direction. Although the instrument was located on a flattened area, which would be expected analytically (ellipsoid model) to result in a smaller MD, the nearby tail structure has a strong influence on the MD. With the tail structure omitted, the calculation predicts an MD value of about 12° . Restoring the tail structure raises the MD to 20° . Lower values of the MD are predicted at other locations on the aircraft (e.g. of order 4° just ahead of the cargo door). The calculations are still in progress and further results will be reported.

The overall agreement between the analytical calculations (e.g. using cylinder and ellipsoid models) and the numbers obtained from the computer model is satisfying. However, it

is evident that more detailed information can be obtained with the computer model calculations. The analytical calculations are limited to simple analytical shapes, whereas with the computer model one can treat more realistic airplane shapes.

NONVERTICAL LIGHTNING CHANNELS

In this section we consider the error in magnetic direction finding due to the effect of nonvertical orientation of a radiating lightning channel, modeled by a radiating dipole tilted away from the vertical. This effect has been analyzed previously (9, 10), but only with the crossed loop detector at ground level. This situation results in important simplifications. The more general case, where the detector is not on the ground but airborne, does not appear to have been considered in the literature. We deal here with the more general case, where both source and observer are above a conducting ground plane. The magnetic crossed-loop detector is considered to be otherwise perfect (no perturbations due to the aircraft, etc.). The "misdirection" due to induced skin currents was treated in the previous section.

Referring to Fig. 6, we consider the detector to be at altitude h above the ground plane (mounted on an aircraft). The lightning radiation source is represented by a dipole of vector dipole moment \vec{P} , located at altitude H above the ground plane. Define a cartesian coordinate system, wherein the ground plane is represented by the x - y plane, and the dipole is centered on the z -axis at a vertical height $z=H$ above the ground plane. The detector is located in the x - z plane, at a height $z=h$ above the ground plane, and at horizontal distance $x=D$ from the z -axis (for $y=0$). Thus, the coordinates of the source and detector in this system are $(0, 0, H)$ and $(D, 0, h)$, respectively. Let R_1 denote the distance from the dipole to the detector, and let R_2 denote similarly the distance from the dipole image (at depth H below the ground plane) to the same detector. Then R_1 and R_2 are given by $R_1^2 = D^2 + (H-h)^2$ and $R_2^2 = D^2 + (H+h)^2$. Let the dipole be arbitrarily oriented, with components P_x , P_y , and P_z . We can then compute the magnetic field as the superposition of contributions from the 3 separate vector dipoles of moments $P_x \hat{i}$, $P_y \hat{j}$, and $P_z \hat{k}$, where \hat{i} , \hat{j} , and \hat{k} denote unit vectors in the x , y and z directions.

According to Hertz' solution of Maxwell's equations, the electric and magnetic fields due to a radiating dipole may be expressed in terms of a dipole moment vector function (11, 12). If we denote the Hertzian time-dependent function by $\vec{P}(t-R/c)$, the vector potential \vec{A} may be written as

$$\vec{A} = \frac{1}{R} \dot{\vec{P}}(t-R/c) \quad (16)$$

where the argument denotes the retarded time at distance R from the dipole, and the dot denotes

differentiation with respect to the time. Here, the units adopted are Gaussian and $\dot{\vec{P}}$ is expressed in emu, i.e., abamp-cm, with R in cm. (In MKS units, an additional factor $\mu_0/4\pi$ appears on the right side, where μ_0 is the magnetic permeability of free space, $4\pi \times 10^{-7}$ henry/meter; then $\dot{\vec{P}}$ is expressed in ampere-meters, with R in meters.)

Now the magnetic field intensity \vec{B} is given by

$$\vec{B} = \text{curl } \vec{A}(R) = (\vec{R}/R) \times (d\vec{A}/dR) \quad (17)$$

since \vec{A} is a function of R only. Differentiation yields

$$\frac{d\vec{A}}{dR} = -\frac{\dot{\vec{P}}}{R^2} - \frac{\ddot{\vec{P}}}{Rc} \quad (18)$$

where the second term results from the dependence of the time-like argument on R, and we obtain

$$\vec{B} = \vec{M}(R) \times \vec{R} \quad (19)$$

with

$$\vec{M}(R) \equiv \frac{1}{R} \left(\frac{\dot{\vec{P}}}{R^2} + \frac{\ddot{\vec{P}}}{Rc} \right) = \alpha \dot{\vec{P}} + \beta \ddot{\vec{P}} \quad (20)$$

so that $\alpha \equiv 1/R^3$ and $\beta \equiv 1/cR^2$.

In terms of our cartesian coordinates, let

$$\begin{aligned} \vec{M}_1 &= M_{1x} \hat{i} + M_{1y} \hat{j} + M_{1z} \hat{k} \\ \vec{M}_2 &= M_{2x} \hat{i} + M_{2y} \hat{j} + M_{2z} \hat{k} \\ \vec{R}_1 &= D \hat{i} - (H-h) \hat{k} \\ \vec{R}_2 &= D \hat{i} + (H+h) \hat{k} \end{aligned} \quad (21)$$

where \hat{i} , \hat{j} and \hat{k} denote unit vectors in the x, y and z directions; and \vec{M}_1 and \vec{M}_2 denote $\vec{M}_1(R_1)$ of the original dipole, and $\vec{M}_2(R_2)$ refers to its image, respectively. In this case, the components of $\dot{\vec{P}}_2$, $\ddot{\vec{P}}_2$ are related to those of $\dot{\vec{P}}_1$, $\ddot{\vec{P}}_1$ by:

$$\begin{aligned} \dot{P}_{2x} &= -\dot{P}_{1x} \equiv -\dot{P}_x & \ddot{P}_{2x} &= -\ddot{P}_{1x} \equiv -\ddot{P}_x \\ \dot{P}_{2y} &= -\dot{P}_{1y} \equiv -\dot{P}_y & \ddot{P}_{2y} &= -\ddot{P}_{1y} \equiv -\ddot{P}_y \\ \dot{P}_{2z} &= +\dot{P}_{1z} \equiv +\dot{P}_z & \ddot{P}_{2z} &= +\ddot{P}_{1z} \equiv +\ddot{P}_z \end{aligned} \quad (22)$$

where we identify the unsubscripted variables with the original dipole. It follows from Eqs. (19) and (21) that, at the observer's position, the magnetic field of the original dipole is given by

$$\begin{aligned} \vec{B}_1 &= [-(H-h)M_{1y}] \hat{i} \\ &+ [(H-h)M_{1x} + D M_{1z}] \hat{j} \\ &+ [-D M_{1y}] \hat{k} \end{aligned} \quad (23)$$

while the magnetic field due to the image is given by

$$\begin{aligned} \vec{B}_2 &= [(H+h)M_{2y}] \hat{i} \\ &+ [-(H+h)M_{2x} + D M_{2z}] \hat{j} \\ &+ [-D M_{2y}] \hat{k} \end{aligned} \quad (24)$$

Hence, the sum of the two fields is:

$$\begin{aligned} \vec{B} &= \vec{B}_1 + \vec{B}_2 \\ &= [(M_{2y} - M_{1y})H + (M_{2y} + M_{1y})h] \hat{i} \\ &+ [-(M_{2x} - M_{1x})H - (M_{2x} + M_{1x})h \\ &+ (M_{2z} + M_{1z})D] \hat{j} \\ &+ [-(M_{2y} + M_{1y})D] \hat{k} \end{aligned} \quad (25)$$

For a vertical dipole, all components of \vec{M}_1 and \vec{M}_2 vanish except for M_{1z} and M_{2z} . Then \vec{B} has only a y component, and there is no misdirection. When \vec{B} has an x-component also, the misdirection angle is given by the arc tangent of $-B_x/B_y$ (Fig. 6b). Consider the ratio $-B_x/B_y$, obtained from Eq. (25):

$$-\frac{B_x}{B_y} = \frac{-(M_{2y} - M_{1y})H - (M_{2y} + M_{1y})h}{-(M_{2x} - M_{1x})H - (M_{2x} + M_{1x})h + (M_{2z} + M_{1z})D} \quad (26)$$

Using Eqs. (20) and (22), we may rewrite Eq. (26) as:

$$-\frac{B_x}{B_y} = \frac{p_y \dot{H} + q_y \ddot{h}}{p_x \dot{H} + q_x \ddot{h} + p_z \dot{D}} \quad (27)$$

where

$$\begin{aligned} p_x &= (\alpha_2 + \alpha_1) \dot{P}_x + (\beta_2 + \beta_1) \ddot{P}_x \\ p_y &= (\alpha_2 + \alpha_1) \dot{P}_y + (\beta_2 + \beta_1) \ddot{P}_y \\ p_z &= (\alpha_2 + \alpha_1) \dot{P}_z + (\beta_2 + \beta_1) \ddot{P}_z \\ q_x &= (\alpha_2 - \alpha_1) \dot{P}_x + (\beta_2 - \beta_1) \ddot{P}_x \\ q_y &= (\alpha_2 - \alpha_1) \dot{P}_y + (\beta_2 - \beta_1) \ddot{P}_y \end{aligned} \quad (28)$$

and where $\dot{P}_x, \ddot{P}_x, \dot{P}_y, \ddot{P}_y, \dot{P}_z, \ddot{P}_z$ refer to the original dipole components. Divide through numerator and denominator by $p_z \dot{D}$, and note that we may write:

$$\begin{aligned} \frac{\dot{P}_x}{p_z} &= \frac{P_x}{P} \frac{\dot{P}}{P}, & \frac{\ddot{P}_x}{p_z} &= \frac{P_x}{P} \frac{\ddot{P}}{P} \\ \frac{\dot{P}_y}{p_z} &= \frac{P_y}{P} \frac{\dot{P}}{P}, & \frac{\ddot{P}_y}{p_z} &= \frac{P_y}{P} \frac{\ddot{P}}{P} \\ \frac{\dot{P}_z}{p_z} &= \frac{P_z}{P} \frac{\dot{P}}{P}, & \frac{\ddot{P}_z}{p_z} &= \frac{P_z}{P} \frac{\ddot{P}}{P} \end{aligned} \quad (29)$$

where P_x, P_y, P_z are the original dipole moment vector components, and where P and \dot{P} are the time derivatives of the vector magnitude P .

Then $p_x/p_z, p_y/p_z, q_x/p_z,$ and q_y/p_z become, using Eqs. (28) and (29):

$$\begin{aligned} \frac{p_x}{p_z} &= \frac{P_x}{P_z}, & \frac{p_y}{p_z} &= \frac{P_y}{P_z} \\ \frac{q_x}{p_z} &= Q \frac{P_x}{P_z}, & \frac{q_y}{p_z} &= Q \frac{P_y}{P_z} \end{aligned} \quad (30)$$

where

$$Q \equiv \frac{(\alpha_2 - \alpha_1) \dot{P} + (\beta_2 - \beta_1) \ddot{P}}{(\alpha_2 + \alpha_1) \dot{P} + (\beta_2 + \beta_1) \ddot{P}} \quad (31)$$

$$= \frac{(1/R_2^3 - 1/R_1^3) \dot{P} + (1/R_2^2 - 1/R_1^2) \ddot{P}/c}{(1/R_2^3 + 1/R_1^3) \dot{P} + (1/R_2^2 + 1/R_1^2) \ddot{P}/c}$$

In the case of harmonic radiation, of angular frequency ω , we may replace \dot{P} by $j\omega P$ in Eq. (31), so that Q is given by the complex quantity, with $k \equiv \omega/c$:

$$\begin{aligned} Q &= - \frac{(x_1^3 - x_2^3) + jk(x_1^2 - x_2^2)}{(x_1^3 + x_2^3) + jk(x_1^2 + x_2^2)} \\ &= - \frac{a + jb}{a' + jb'} \end{aligned} \quad (32)$$

where

$$\begin{aligned} x &= 1/R & (x_1 = 1/R_1, & x_2 = 1/R_2) \\ a &= x_1^3 - x_2^3 & b &= k(x_1^2 - x_2^2) \\ a' &= x_1^3 + x_2^3 & b' &= k(x_1^2 + x_2^2) \end{aligned}$$

so that

$$\begin{aligned} Q &= - \frac{(aa' + bb')}{(a')^2 + (b')^2} + \frac{j(ab' - ba')}{(a')^2 + (b')^2} \\ &= \text{Re } Q + j \text{Im } Q \end{aligned} \quad (33)$$

Finally, the ratio $-B_x/B_y$ may be written:

$$-\frac{B_x}{B_y} = \frac{G \frac{P_y}{P_z}}{1 + G \frac{P_x}{P_z}} \equiv \tan(\text{MD}) \quad (34)$$

where MD is the misdirection angle and where G is a geometrical factor:

$$G \equiv \frac{H + Qh}{D} \quad (35)$$

If the detector is on the ground plane ($h=0$), the problem simplifies greatly, and we have $\alpha_1=\alpha_2$ and $\beta_1=\beta_2$, so that $Q=0$. Then G reduces simply to $G=H/D$, and we have

$$-\frac{B_x}{B_y} = \frac{\frac{H}{D} \frac{P_y}{P_z}}{1 + \frac{H}{D} \frac{P_x}{P_z}} \quad (36)$$

which is identical to the result given by Uman et al (Ref. 10 - see plots), re-expressed in our terms, for a detector on the ground plane. An equivalent result was also given earlier for this case by Kalakowsky and Lewis (9).

If the ground plane is completely nonconducting (no image), then the case of the detector at altitude h above ground also simplifies greatly. In this case α_2 and β_2 vanish, and $Q=-1$. Then

$$-\frac{B_x}{B_y} = \frac{\frac{(H-h)}{D} \frac{P_y}{P_z}}{1 + \frac{(H-h)}{D} \frac{P_x}{P_z}} \quad (37)$$

That is, H is replaced in Eq. (36) by the "net altitude," $H-h$.

A geometric interpretation of Eq. (36) (or (37)) is obtained by rewriting Eq. (34) in the form, assuming $Q=0$:

$$(D + H \frac{P_x}{P_z}) B_x + H \frac{P_y}{P_z} B_y = 0 \quad (38)$$

This expression implies that the "misdirection," in the plane of the observer and perpendicular to \vec{E} at the observer, passes through the point whose x, y, z coordinates are $-(P_x/P_z)H$, $-(P_y/P_z)H$, and zero. This point (indicated by the letter I in Fig. 6a) is also the intercept of the extended line of the dipole with the $z=0$ plane. This simple geometric interpretation for a detector on a conducting ground plane was pointed out by Kalakowsky and Lewis (9).

The correction factor for finite aircraft altitude is given by the term Qh in Eq. (35). Assuming a frequency of 50 kHz (Stormscope central frequency), a lightning distance 15 km ($=D$), a lightning altitude 3 km ($=H$), and aircraft altitude 3 km ($=h$), we obtain from Eq. (33) the approximate value $-1/3$ for $\text{Re } Q$. Thus, for this case the geometrical factor G is reduced to about $2/15$ compared with its zero-altitude ($h=0$) value of $3/15$.

APPENDIX. USE OF ELECTRIC ANTENNA TO RESOLVE 180-DEGREE AMBIGUITY

A simple way of seeing how correlation of the phases of the electric and magnetic vectors can be used to resolve the ambiguity is the following.

Consider one loop of a narrowband crossed-loop system aligned with two sources, one in "front" and one in "back". In Fig. A-1, the plane of the loop is perpendicular to the plane of the paper and is aligned with the sources (upper dot = front, lower dot = back). The sources are assumed to be electric dipoles in the same plane as the detector, but oriented perpendicular to the plane of the paper. Four sets of vectors are shown, at (a), (b), (c) and (d), with E, H , and P in each set denoting, respectively, the electric vector, magnetic vector, and direction-of-propagation vector, respectively. Sets (a) and (b) correspond to radiation from the front, while sets (c) and (d) correspond to radiation from the back. Let signs be associated with E and H , such that E pointing upward and downward denotes a positive and negative amplitude, respectively. While H pointing right and left denotes also a positive and negative amplitude, respectively (readily convertible into loop voltage signs). The four possibilities may be tabulated as follows:

	<u>E</u>	<u>H</u>	<u>Source</u>
a)	-	+	front
b)	+	-	front
c)	-	-	back
d)	+	+	back

It is evident from the table that E and H have opposite signs if the source is in front, while they have the same signs if the source is in back. It is not difficult to apply the same procedure to the second loop.

Thus it is readily seen why electrical noise can produce 180° errors. If the signal-to-noise ratio is too low or the electronics is ineffective, electrical noise pulses of the wrong sign can overwhelm the electric field amplitude and make it appear, say, negative when it should be positive, and vice versa. Similar errors may be caused by unintentional phase shifts in the signal amplifiers.

ACKNOWLEDGMENT

This work was supported by the Air Force.

REFERENCES

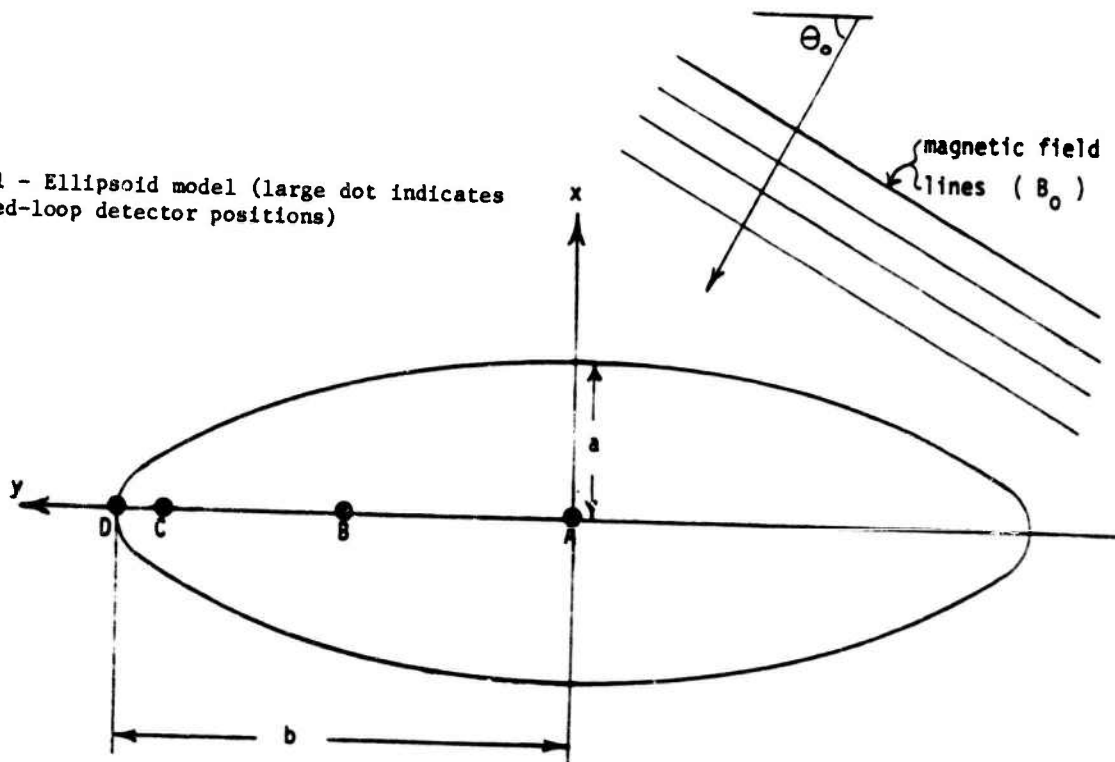
1. L. W. Parker and H. W. Kasemir, "Airborne Warning Systems for Natural and Aircraft-Initiated Lightning," IEEE Transactions on Electromagnetic Compatibility, Vol. EMC-24, No. 2, pp. 137-158, May 1982.
2. L. W. Parker and H. W. Kasemir, "Airborne Lightning Warning Systems: A Survey," Lee W. Parker, Inc. Final Report to Air Force Geophysics Laboratory, AFGL-TR-80-0226, July 1980.
3. These errors are equivalent to the well-known "quadrantal" bearing errors (difference between true and apparent directions) that are normally compensated in the design of low-frequency ADF loop antennas for aircraft. See for example "Antenna Engineering Handbook," pp. 27-10, 11, 12, H. Jasik, editor, New York: McGraw-Hill, 1961.
4. T. J. Seymour and R. K. Baum, "Evaluation of the Ryan Stormscope as a Severe Weather Avoidance System for Aircraft - Preliminary Report," Report FAA-RD-79-6, pp. 29-35, FAA/FIT Workshop on Grounding and Lightning Technology, Melbourne, Florida, 1979.
5. R. K. Baum and T. J. Seymour, "In-Flight Evaluation of a Severe Weather Avoidance System for Aircraft," Air Force Flight Dynamics Laboratory Report AFWAL-TR-80-3022, May 1980.
6. J. Reazer, "Data Acquisition for Evaluation of an Airborne Lightning Detection System," Air Force Flight Dynamics Laboratory Draft Report, to be published in Spring of 1983.
7. J. A. Stratton, "Electromagnetic Theory," New York: McGraw-Hill, 1941.
8. C. E. Baum, personal communication.
9. C. B. Kalakowsky and E. A. Lewis, "VLF Sferics of Very Large Virtual Source Strength," Air Force Cambridge Research Laboratories Report AFCRL-66-629, 1966.
10. M. A. Uman, Y. T. Lin and E. P. Krider, "Errors in Magnetic Direction Finding Due to Non-vertical Lightning Channels," Radio Science, Vol. 15, pp. 35-39, 1980.
11. M. Abraham and R. Becker, "The Classical Theory of Electricity and Magnetism," London: Blackie and Son, Ltd., 1937.
12. A. Sommerfeld, "Electrodynamics. Lectures on Theoretical Physics," Vol. 3, New York: Academic Press, 1952.
13. A. Sommerfeld, "Partial Differential Equations in Physics. Lectures on Theoretical Physics," Vol. 6, New York: Academic Press, 1949.

Table 1 - Misdirection (Bearing Error) of Crossed Loop on Spheroidal Fuselage ($MD = \theta - \theta_0$)*

Incident Angle θ_0 (degrees)	Needle (Cylinder) Limit	$t=0.1$	$t=0.2$	$t=0.5$	Sphere
	$t=0.0$ $R=0.5$	$R=0.5207$	$R=0.5591$	$R=0.7100$	Limit $t=1.0$ $R=1.0$
0	0.	0.	0.	0.	0.
5	- 2.50	- 2.39	- 2.20	- 1.45	0.
10	- 4.96	- 4.75	- 4.37	- 2.86	0.
15	- 7.37	- 7.05	- 6.48	- 4.23	0.
20	- 9.69	- 9.26	- 8.50	- 5.51	0.
25	-11.88	-11.34	-10.39	- 6.68	0.
30	-13.90	-13.26	-12.11	- 7.71	0.
35	-15.70	-14.96	-13.62	- 8.57	0.
40	-17.24	-16.39	-14.87	- 9.22	0.
45	-18.43	-17.48	-15.79	- 9.63	0.
50	-19.21	-18.16	-16.33	- 9.76	0.
55	-19.47	-18.35	-16.40	- 9.60	0.
60	-19.11	-17.94	-15.93	- 9.12	0.
65	-18.00	-16.83	-14.83	- 8.30	0.
70	-16.05	-14.94	-13.07	- 7.14	0.
75	-13.19	-12.22	-10.61	- 5.68	0.
80	- 9.43	- 8.70	- 7.51	- 3.95	0.
85	- 4.92	- 4.53	- 3.90	- 2.02	0.
90	0.	0.	0.	0.	0.

* θ = sensed angle; θ_0 = incident angle; t = aspect ratio = ratio of minor to major axes; R = misdirection factor, Eq.(13).

Fig. 1 - Ellipsoid model (large dot indicates crossed-loop detector positions)



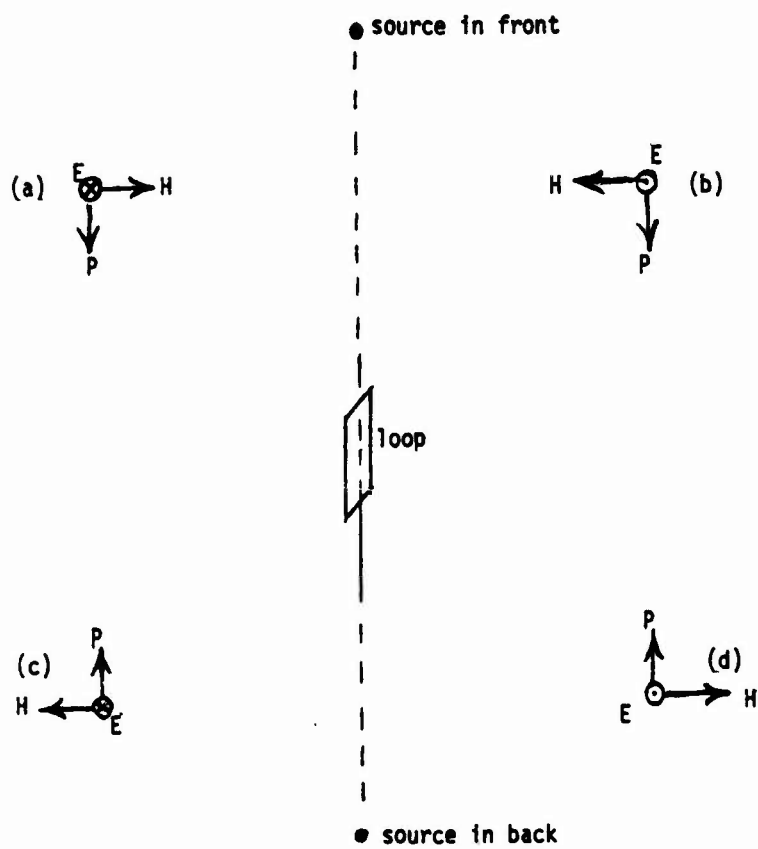


Fig. A-1 - Resolution of the 180-degree ambiguity

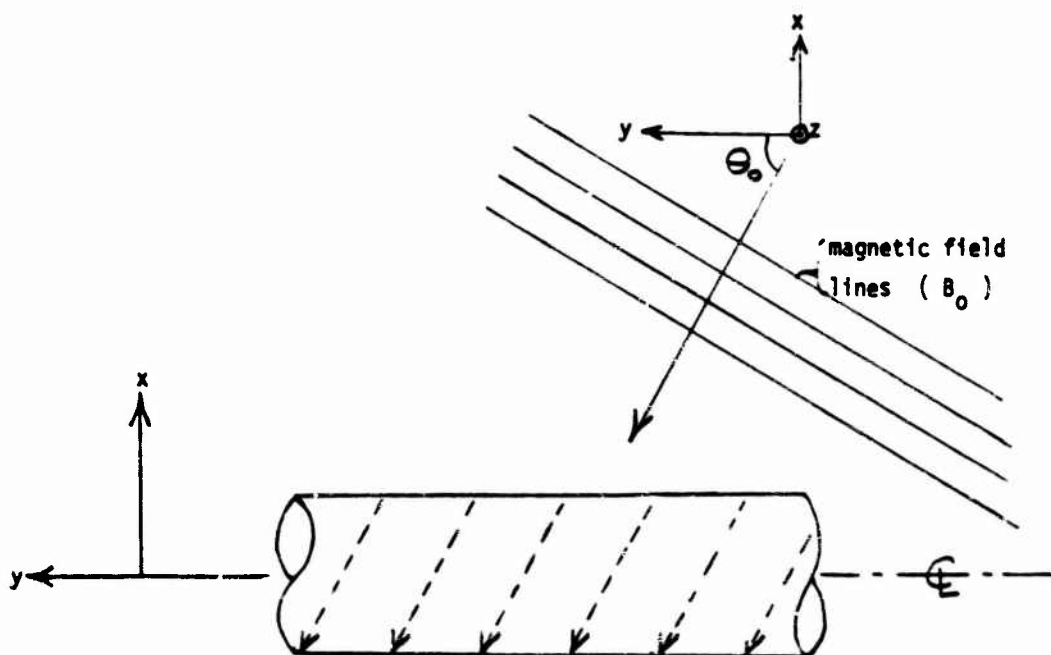


Fig. 2 - Elliptic or circular cylinder (dashed lines indicate current flow planes)

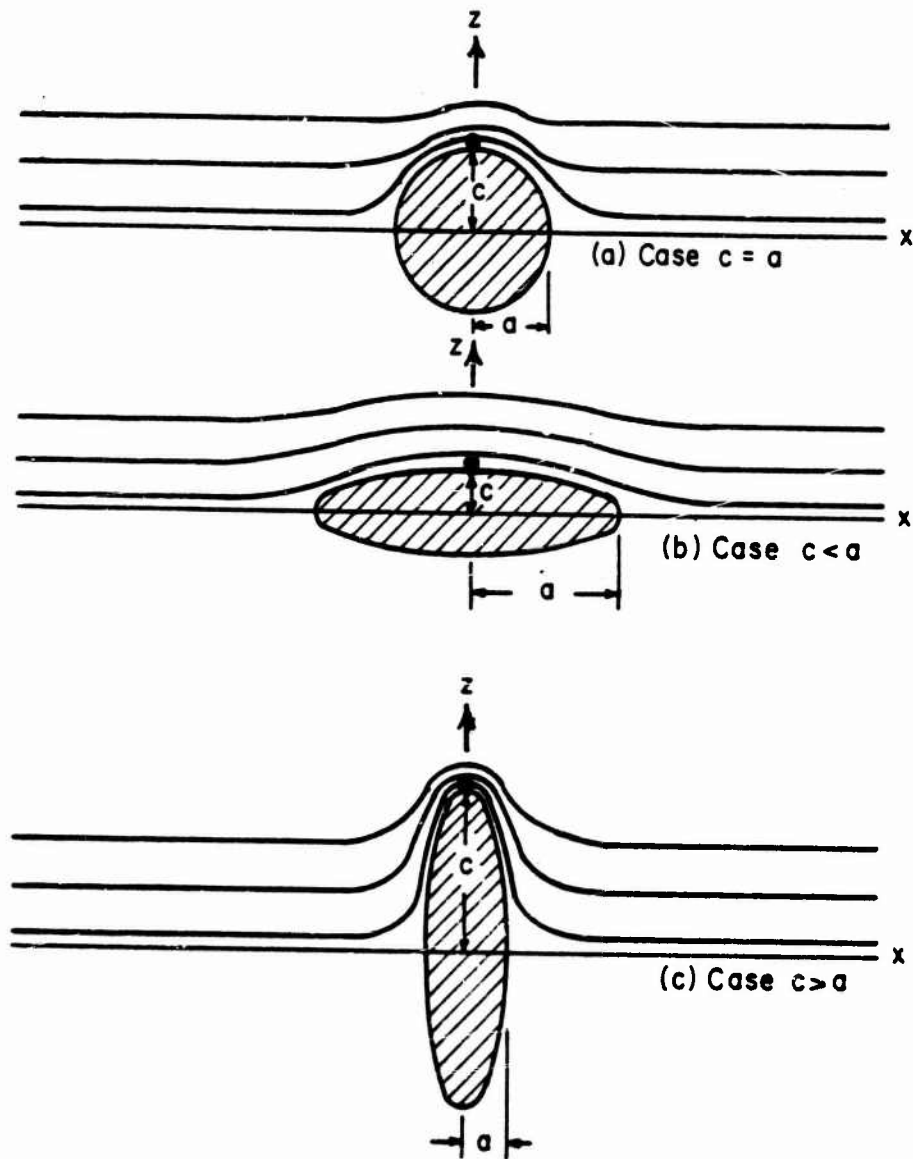


Fig. 3 - Transverse field lines around circular and elliptic cylinders (large dot indicates detector position)

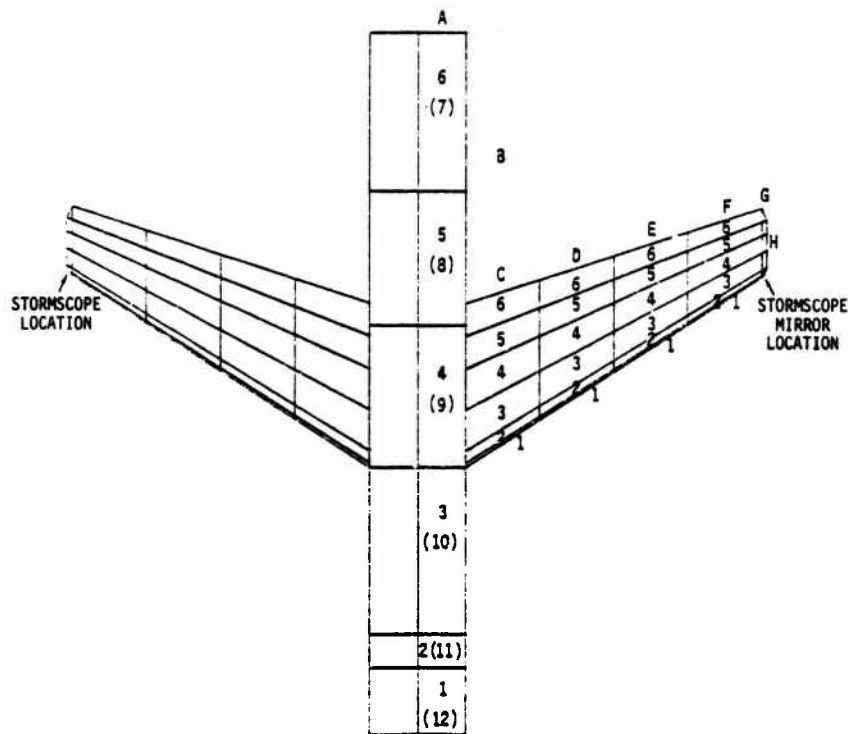


Fig. 4a - T-39 computer model, topside view
 (letters and integers indicate panel locations,
 mirror of Stormscope detector located on Panel
 G-11 directly under Panel G-2)

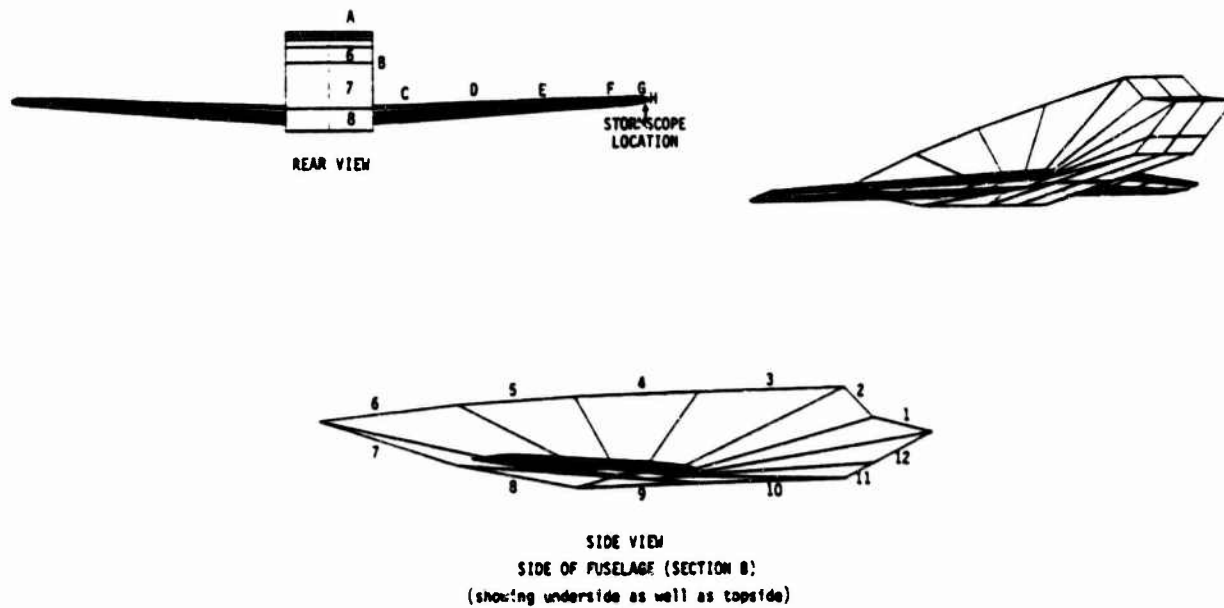


Fig. 4b - T-39 computer model, other views

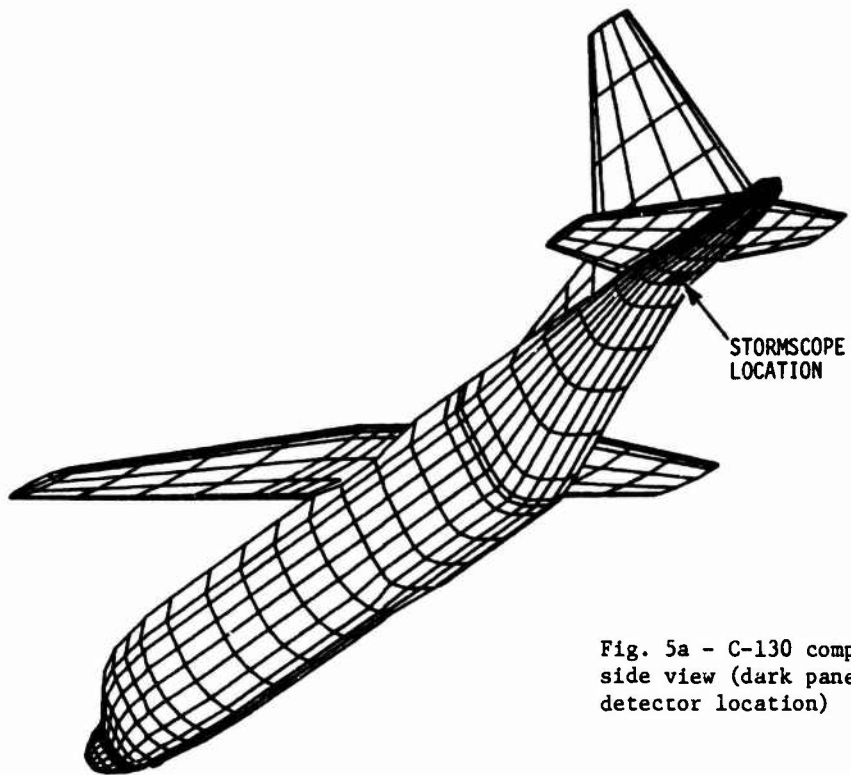


Fig. 5a - C-130 computer model, general underside view (dark panel indicates Stormscope detector location)

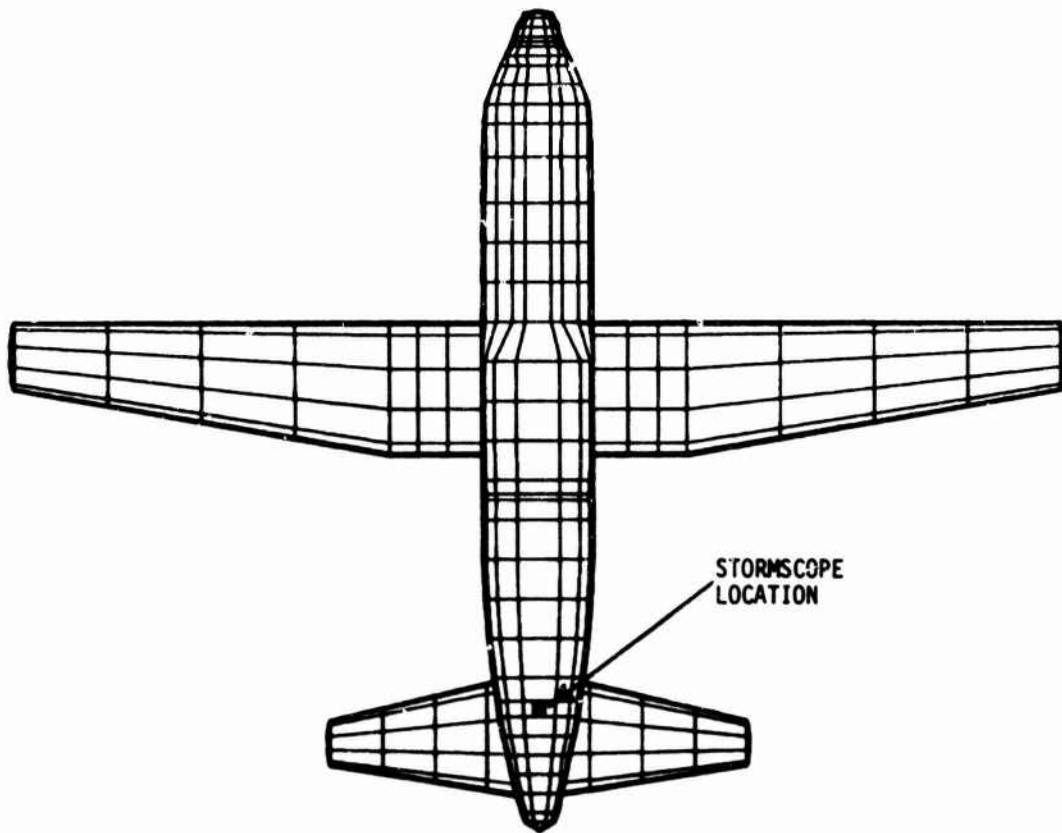


Fig. 5b - C-130 computer model, underside view

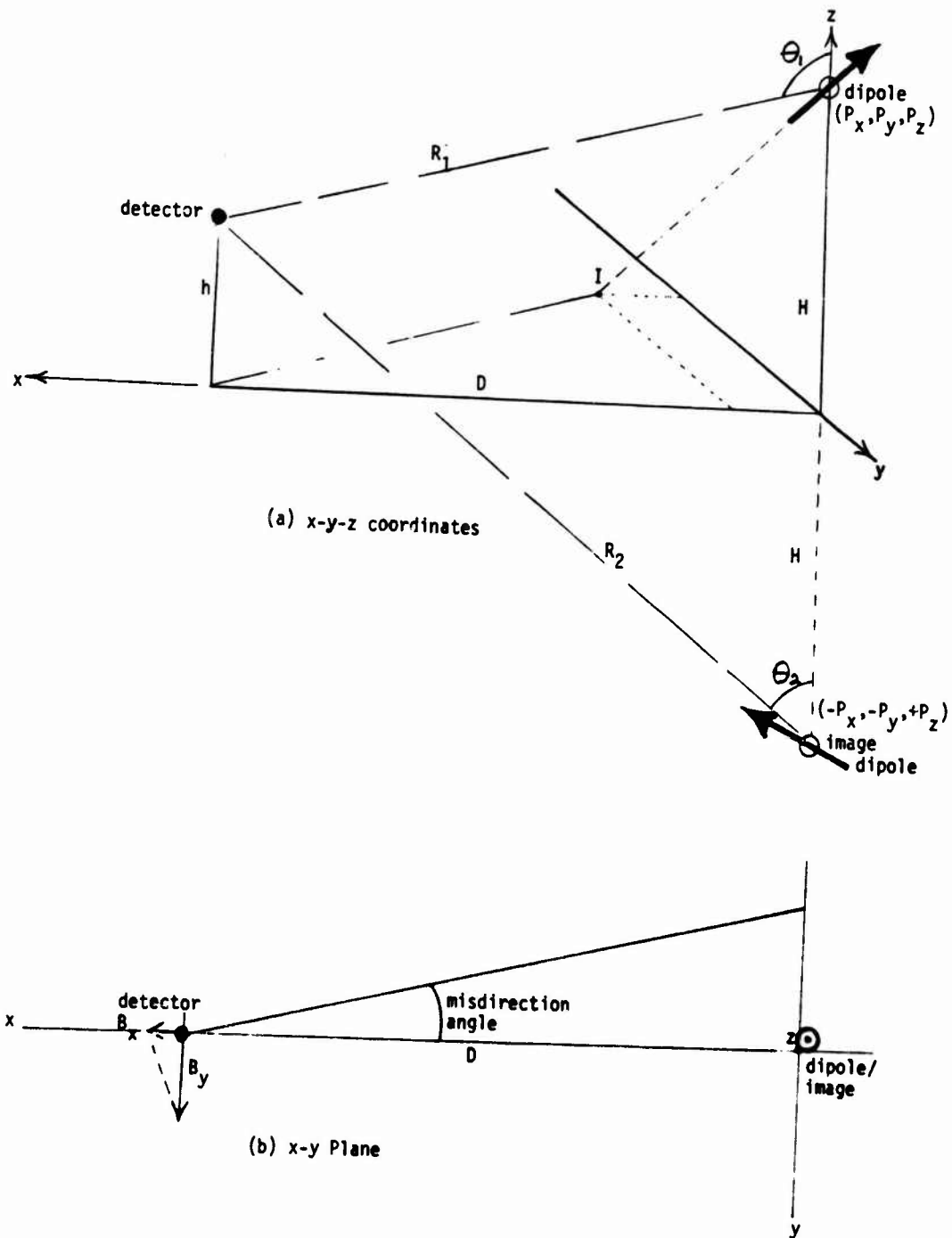


Fig. 6 - Nonvertical dipole and image in conducting ground plane (detector also above ground)